Impact of SO<inf>2</inf> and light on chemical morphology and hygroscopicity of natural salt aerosols

Atmospheric Environment 322 (2024) 120373

Contents lists available at ScienceDirect

Atmospheric Environment

journal homepage: www.elsevier.com/locate/atmosenv

Impact of SO_2 and light on chemical morphology and hygroscopicity of natural salt aerosols

Xiangrui Kong [a,*], Cheng Wu [a], Harsh Raj Mishra [a,b], Yuxin Hao [c], Mathieu Cazaunau [d], Antonin Bergé [e], Edouard Pangui [d], Robin Faust [f], Wanyu Liu [c,#], Jun Li [c,1], Sen Wang [c], Bénédicte Picquet-Varrault [d], Mattias Hallquist [a,**]

[a] Department of Chemistry and Molecular Biology, Atmospheric Science, University of Gothenburg, SE-41390, Gothenburg, Sweden
[b] School of Earth and Atmospheric Sciences, Queensland University of Technology, QLD, 4001, Brisbane, Australia
[c] Department of Environmental Sciences, College of Urban and Environmental Sciences, Northwest University, 710069, Xi'an, China
[d] Univ Paris Est Creteil and Université Paris Cité, CNRS, LISA, F-94010, Créteil, France
[e] Université Paris Cité and Univ Paris Est Creteil, CNRS, LISA, F-75013, Paris, France
[f] Department of Chemistry and Chemical Engineering, Chalmers University of Technology, Kemigården 4, SE-41390, Göteborg, Sweden

HIGHLIGHTS

- Natural salt particles show higher SO_2 uptake than pure NaCl particles.
- The hygroscopicity is influenced by chemical complexity, SO_2 exposure, and light conditions.
- Light exposure suppresses hygroscopic growth, potentially leading to the formation of less hygroscopic species.
- Natural salt particles exhibit rounded shapes with cubic NaCl cores encased in sulfate coatings.
- Particles exhibit morphological and spectral changes after exposure to SO_2, light, and high RH.

ARTICLE INFO

Keywords:
SO2
Salt particles
Chamber
Chemical morphology
STXM
Salt lake
Ionic strength

ABSTRACT

The interactions between SO_2 and natural salt aerosol particles represent complex and crucial dynamics within atmospheric processes and the broader climate system. This study investigated the SO_2 uptake, hygroscopicity, morphology and mixing states of natural salt particles, which are generated from brines sampled from the Chaka salt lake located in the Qinghai-Tibet plateau. A comparison with atomized pure NaCl particles is included as reference. The results show that NaCl particles exhibit the lowest SO_2 uptake, while Chaka salt particles demonstrate higher uptake due to their complex composition. The hygroscopicity of salt particles is influenced by several factors, including chemical complexity, SO_2 exposure and light conditions. In comparison to pure NaCl, Chaka salt displays higher hygroscopicity, which is further enhanced in the presence of SO_2. However, when exposed to light, mass growth is suppressed, suggesting the formation of species with lower hygroscopicity, such as Na_2SO_4. Analysis of particle morphology and mixing states reveals notable distinctions between NaCl crystals and Chaka salt particles, where the Chaka salt particles exhibit rounded shapes with a structure composed of cubic NaCl cores surrounded by sulfate materials as a coating. In addition, the chemical morphology analysis also reveals that the particles show morphological and spectral changes before and after the exposure to SO_2, light and high RH. Therefore, this research highlights the intricate interactions between SO_2 and natural salt aerosol particles in diverse environmental settings, underscoring their multifaceted impacts on atmospheric processes.

* Corresponding author.
** Corresponding author.
E-mail address: kongx@chem.gu.se (X. Kong).
College of Ocean and Earth Sciences, Xiamen University, 361000 Xiamen, China.
1 Beijing Normal University, 100000 Beijing, China.

https://doi.org/10.1016/j.atmosenv.2024.120373
Received 28 October 2023; Received in revised form 23 January 2024; Accepted 29 January 2024
Available online 6 February 2024

1. Introduction

Sulfate is a significant component of atmospheric aerosols, aiding the formation of new aerosol particles through nucleation (Kulmala et al., 2000). The impact of sulfate aerosols on solar radiation scattering and cloud microphysics introduces substantial uncertainties in climate change assessments (Ge et al., 2022; Krishnamohan et al., 2019; Thornhill et al., 2021). The main source of atmospheric sulfate is the oxidation of SO_2 (Seinfeld and Pandis, 2016), which are emitted directly from diverse sources like fossil fuel combustion, industrial processes, and volcanoes, or formed in the atmosphere through the oxidation of reduced sulfur compounds, such as dimethyl sulfide (DMS) (Gondwe et al., 2003), emitted by oceanic phytoplankton (Alcolombri et al., 2015).

Various pathways for sulfate formation are considered in atmospheric models, including gas-phase oxidation of SO_2 by hydroxyl radicals (OH), in-cloud oxidation by hydrogen peroxide (H_2O_2), ozone (O_3), hypochlorous and hypobromous acids (HOCl and HOBr), as well as multiphase oxidation of SO_2 by O_3 and HOCl in salt aerosols (Alexander et al., 2005). The oxidation in the aqueous phase is considered to occur primarily within clouds due to their high liquid water content (Cheng et al., 2016; Quan et al., 2015), which differs in urban aerosols or deliquescent salt aerosols (Elser et al., 2016). However, it has been recently reported that deliquescent salt and dust aerosols could serve as important sites for aqueous phase sulfate production (Wang et al., 2022b), attributed to the rapid rate of SO_2 oxidation by ozone in alkaline solutions (Harris et al., 2012). It is found that the sulfate formation rate for the O_3 oxidation pathway is accelerated by two orders of magnitude under high ionic strength conditions compared to dilute bulk solutions, which indicates that ionic strength plays a crucial role in sustaining the importance of the multiphase oxidation of SO_2 by O_3 in salt aerosols (Chen et al., 2022; Yu et al., 2023). In addition, transition metals also catalyze SO_2 to form sulfate, and recent studies suggest that the transition metal-catalyzed oxidation of SO_2 on aerosol surfaces could be the dominant pathway for sulfate formation (Wang et al., 2021, 2022a).

Apart from aqueous chemistry, heterogeneous SO_2 oxidation and sulfate formation pathway on dust and salt surfaces are also potentially important. A recent study reported that certain components present on the surface of dust particles, such as Fe, Ti, Al, NaCl, KCl, and Ca^{2+}, are associated with the heterogeneous formation of sulfate (Wang et al., 2022b). Another study investigated the formation of sulfites and sulfates on the surfaces of volcanic and desert dust, and the results demonstrated that the surface composition of the dust particles plays a role in determining the amounts of sulfites and sulfates formed when RH is below 30%. Specifically, increased levels of sulfites are directly correlated with the ratio of (Fe + Ti) to Si, while elevated levels of sulfates are linked with the presence of Na on the dust surface (Urupina et al., 2022). The findings suggest that the SO_2 oxidation may be related to the catalytic effects of alkali metals (Kong et al., 2023), as alkali metals have been recognized as catalysts in biomass thermal conversion processes (Yu et al., 2021).

Given the existing uncertainties about SO_2 oxidation, it is crucial to recognize the substantial contribution of salt particles. In addition to their well-established functions in atmospheric chemistry and the climate system, these salt particles serve as indispensable entities in the intricate processes of aerosol and cloud formations. Their significant ability to attract and absorb water vapor from the atmosphere allows them to play a crucial role in the complex interactions between aerosols and clouds (Randles, 2004). Moreover, the salt particles have the capacity to provide high ionic strength and influence gas-particle partitioning of important trace gases (Kampf et al., 2013; Pratap et al., 2021).

Salt particles can be generated through diverse pathways, including sea spray, wind erosion, and anthropogenic activities like biomass burning. Saline lakes and playas play a pivotal role as noteworthy reservoirs of salt particles (Gaston et al., 2017), which can undergo long-range transport (Ghomashi and Khalesifard, 2020; Osler, 2012). The interconnectivity of these particles and their consequential impact on atmospheric processes and environmental dynamics hold particular significance in the context of climate change (Kelly et al., 2007). Naturally sourced salt aerosol particles typically exist as complex mixtures (Liu et al., 2021; Olson et al., 2019), with their morphology and mixing states exerting considerable influence on their physicochemical attributes (Olson et al., 2019; Sullivan et al., 2009). Nonetheless, the comprehensive characterization of their morphology and mixing states remains limited. It is worth noting that the morphology and mixing states of salt particles exert direct influence on various crucial physicochemical properties (Dommer et al., 2023), including hygroscopicity, which is dictated by the composition of the surface materials (Laskina et al., 2015; Lee et al., 2020; Li et al., 2016).

In this study, the investigation involves examining the uptake and transformation of SO_2 gas on both natural salt aerosol particles and NaCl particles within an atmospheric simulation chamber. It is necessary to investigate the interaction of SO_2 with natural salt aerosols, as these aerosols are directly relevant and more complex compared to simplified models or individual compounds like NaCl. The morphology and mixing states of natural salt aerosol particles are examined using synchrotron-based scanning transmission X-ray microscopy (STXM). A comparative analysis is conducted with NaCl, a chloride salt possessing distinct cationic composition and crystalline structure. The impact of SO_2 exposure on the hygroscopic properties of both natural salt and NaCl particles is explored, which reveals that the SO_2 uptake and its effects on salt aerosol transformation is influenced by light conditions and the chemical compositions.

2. Materials and experimental

2.1. Material and sampling site

The material used in this study is a natural brine obtained from Chaka (CK) Lake (Xingqi et al., 2008), situated in the Qaidam Basin on the Qinghai-Tibet Plateau, as depicted in Fig. 1. The Qinghai-Tibet Plateau is renowned for its elevated altitude and is often referred to as the "roof of the world." Spanning approximately 300 square kilometers, Chaka Lake represents one of the largest saltwater lakes in the region.

The sample brine was collected from a depth of 2–5 cm below the lake surface September 12th, 2020. The brine was then filtered using qualitative filter papers with a pore size of less than 20 μm within 48 h of sampling. After filtration, the sample was stored in polyethylene bottles, sealed with Parafilm membrane, and refrigerated at 4 °C until measurements were taken. The ionic composition of the brine was characterized by ion cryotomography (IC), and the results have been

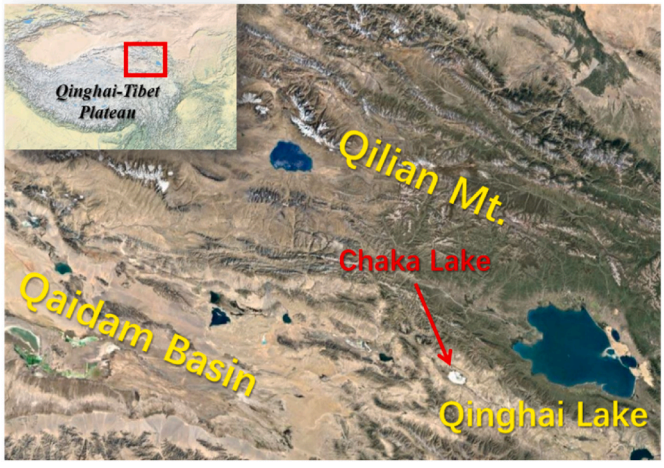

Fig. 1. The sampling site, Chaka Lake (36°43′53″N, 99°4′43″E), and its location in the Qinghai-Tibet Plateau.

previously reported and here presented in Table 1 (Liu et al., 2021). The results show that the CK brine contains Cl^-, Na^+, Mg^{2+} and SO_4^{2-} as the main ions. As a reference material, pure NaCl (Suprapur, ≥99.5%, Merck KGaA) is used for comparison. The highly saline environment presents a challenge for most organic life forms, therefore the organic content in salt lakes is usually lower compared to freshwater lakes or oceans.

2.2. Chamber experiments

The chamber experiment was carried out at the CESAM chamber in Paris. The chamber is a stainless-steel vessel with a volume of 4.2 m^3, temperature and pressure controlled and equipped with solar simulator lamps (Wang et al., 2011). The reaction volume within the chamber is irradiated using three high-powered arc xenon lamps, each with an output of 7 kW (MHDiffusion®), positioned above the chamber. The irradiation is conducted through three quartz windows. These lamps are specifically chosen for their ability to emulate the solar actinic flux, both in terms of spectral distribution and intensity, offering a close approximation to natural sunlight conditions. The actinic flux emitted by these lamps is compared to solar flux values, which are calculated using the TUV/NCAR model for a latitude of 40°, specifically on June 30th at 3 p.m. (Fig. S1 in the *Supporting Information*). Aerosol lifetimes in CESAM are up to 4 days, allowing investigating aerosol ageing and multiphase chemistry. The chamber is equipped with dedicated analytical instruments for gas and aerosol phases. It is coupled to an *in situ* long path FTIR spectrometer (Bruker Tensor 37), an *in situ* long path UV–visible spectrometer, a high-resolution PTR-ToF-MS (Kore Series 2e, mass resolution of 4000) and gas monitors (SO_2, NOx, O_3, CO/CO_2). The size distribution of the particle phase is measured with a scanning mobility particle sizer (SMPS) composed of a TSI classifier model 3080 and differential mobility analyzer (DMA) model 3081 coupled to a condensation particle counter (CPC) TSI model 3772 which allowed measurements in the range of 20–880 nm. The size distribution of larger particles is measured with a Palas Welas (Welas digital 2000) which allows covering the size range 0.2–17 μm.

2.3. Experimental procedure

Prior to the experiments, the chamber was pumped down to few 10^{-4} mbar for the entire night for cleaning. Then it was filled with a mixture of high-purity N_2/O_2 (80/20) and maintained at a pressure just above ambient for the duration of the experiment. A typical experiment is shown in Fig. 2a. First, salt particles were generated using an atomizer and dried prior to injection into the chamber. Note that different particle generating methods can influence the physicochemical properties of the aerosols. For instance, compared to natural oceanic processes, atomizers may produce particles with distinct chemical compositions, shapes, and hygroscopic growth behaviors. These properties may impact the interaction between the particles with other atmospheric components as well as their light-scattering abilities (Zieger et al., 2017). Once the mass concentration reached approximately 50 μg/m^3, the aerosol injection was stopped, followed by a mass concentration decline due to continuous dilution (by instrument sampling) and wall loss. Then, 100 ppb SO_2 was injected, and the RH was gradually increased in steps by injecting water vapor using a stainless-steel boiler. The RH was then maintained at a constant value by passing nitrogen through a heated water bubbler.

Fig. 2b shows the rapid decrease of SO_2 concentration after the injection. It is worth noting that the measured SO_2 concentration is influenced by the RH, as indicated by a simultaneous increase in SO_2 levels when the RH reaches 20%. A similar, albeit smaller, increase in SO_2 was observed when the RH further rose to 50%. However, when the RH reached 70%–80%, the SO_2 concentration decreased. A detailed analysis of the effects of RH on SO_2 concentration is provided in the *Supporting Information* (Fig. S2).

Fig. 2c exhibits the time series of size distributions measured by the SMPS. As soon as the aerosol injection stopped, the smaller particles vanished immediately. This disappearance is attributed primarily to

Table 1
Ion concentrations of the Chaka brine determined by IC.

Ion concentration (per liter)						
Na^+	K^+	Mg^{2+}	Ca^{2+}	Cl^-	SO_4^{2-}	NO_3^-
2.658 mol	0.095 mol	0.906 mol	0.002 mol	4.603 mol	0.280 mol	0.001 mol
61.130 g	3.708 g	21.752 g	0.096 g	16.340 g	26.908 g	0.064 g

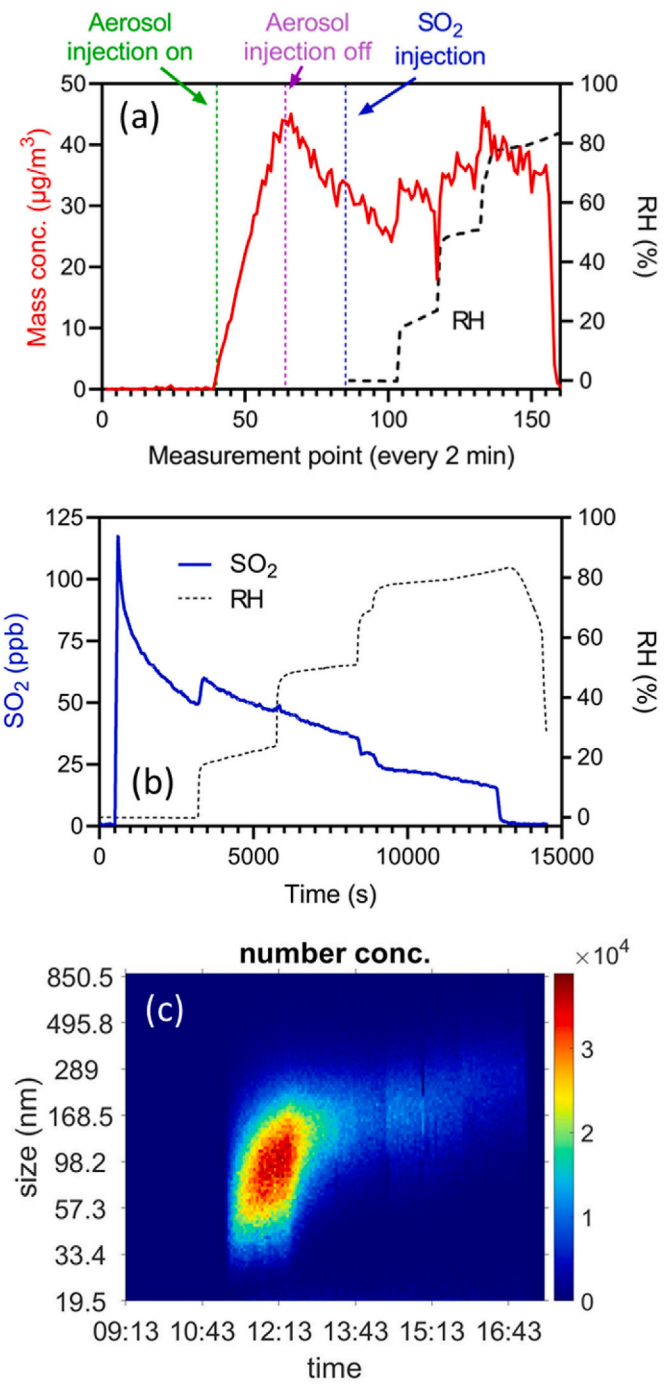

Fig. 2. (a) Mass concentrations and RH in an example experiment, where the onset and stop of the aerosol and SO_2 injections are indicated. (b) Time series of SO_2 after injection, including RH steps. (c) Time series of size distributions of number concentration, with the unit for the color bas is number per m^3.

coagulation and diffusion-induced wall loss, which have a more pronounced effect on smaller particles. Note that these example time series are raw data before the corrections for dilution and wall loss. For light conditions, the solar-simulating bulbs were switched on right after the aerosol injection was finished. The ozone concentration was monitored continuously, and none of the cases studied here show the formation of ozone. The list of experiments is presented in Table 2, together with the experimental conditions. Several control experiments were also performed by injecting SO_2 alone (exp. 6), by injecting the Chaka salt aerosol alone (exp. 1) and by replacing Chaka salt by NaCl aerosol (exp. 5).

2.4. Dilution correction

2.4.1. Correction for dilution

To maintain constant pressure in the chamber, a compensation system is employed during air sampling, which also leads to the dilution of the mixture. Consequently, the collected data needs to undergo correction. The formula used for correcting the dilution effect is as follows:

$$m(t)_{corr} = m(t-1)_{corr} + \Delta m_{meas} + \frac{Q_p}{V} \times m(t-1)_{meas} \times e^{-\frac{Q_p}{V}} \Delta t$$

with $m(t)_{corr}$ represents the corrected amount (mass, concentration, etc.) at time t, $m(t-1)_{corr}$ signifies the corrected amount at time t-1, Δm_{meas} denotes the difference between the measured amounts at time t and t-1, Q_p (L/min) represents the sampling flow rate, V represents the volume of the chamber (L), $m(t-1)_{meas}$ represents the non-corrected amount at time t-1, and Δt represents the time interval between t-1 and t.

2.4.2. Correction for particle physical wall loss

In order to account for the deposition of particles onto the chamber walls, a correction needs to be applied to address the physical wall loss. A previous study has indicated that the deposition rate primarily depends on the particle size rather than their chemical composition (K. Lai and Nazaroff, 2000). In the CESAM chamber, the deposition rate was measured as a function of particle diameter through controlled experiments using ammonium sulfate particles with a density of 1.77 g/cm^3.

Once the deposition coefficient (k_w) has been determined based on aerosol diameter, the formula used to correct the particle number concentration is as follows:

$$N_{\mathrm{corr}}(t) = N_{meas}(t) + k_w \int_0^t N_{\mathrm{meas}} dt$$

It is important to note that the physical wall loss of particles in the CESAM chamber is relatively minimal (<10%) on the typical timescale of an experiment.

2.5. Individual particle sampling and chemical mapping measurements

The combination of scanning transmission X-ray microscopy (STXM) and near edge X-ray absorption fine structure (NEXAFS) analysis is advantageous in both high energy and spatial resolutions, which can be used to chemically map the mixing states of different elements and functional groups. A 5-stage Sioutas cascade impactor was used to collect particle samples at a flow rate of 9 L/min. To optimize particle collection efficiency and guarantee the availability of appropriately sized particles for STXM analysis, the fifth stage of the impactor was exclusively utilized, which targets particles with a diameter of 0.25 μm or larger. During each sampling phase, a Transmission Electron Microscopy (TEM) grid (Carbon Type B film from Ted Pella, Inc.) was installed in the fifth stage to gather the particles. The samplings were carried out at different RH conditions (0%, 20%, 50%, 80%) in the chamber. Once collected, the samples were placed in sealed containers until STXM analysis. The collected particle samples were inspected and analyzed at the BL4U beamline at the UVSOR synchrotron facility in Okazaki, Japan (Ohigashi et al., 2013). STXM/NEXAFS measurements were performed at the oxygen K-edge, chlorine L-edge, sulfur L-edge, carbon K-edge, potassium L-edge, nitrogen K-edge and calcium L-edge. The spatial resolution capability of STXM is 50 nm. Data analysis, including image alignments, selection of background regions and conversion of transmitted flux data was performed using AXIS 2000. In addition, the samples were investigated with scanning electron microscopy (SEM) using a Quanta 200 FEG. The selected acceleration voltage was 10 kV, and the secondary electron signal was used for imaging. Energy dispersive X-ray spectroscopy (EDX) analysis was conducted to measure the concentration of S in the particles.

Table 2
Summary of chamber experiments.

Experimental No.	Aerosol type	RH (%)	SO_2 (ppb)	Light	Mass (μg•m^{-3})	STXM samples
1	Chaka salt	0–80%	0	–	55	3
2	Chaka salt	0–80%	100	–	66	5
3	Chaka salt	0–80%	100	–	51	2
4	Chaka salt	0–80%	100	on	49	10
5	NaCl	0–80%	100	–	56	8
6	–	0–80%	100	–	0	0

3. Results and discussions

3.1. SO_2 uptake by natural salt particles and NaCl particles

Based on the understanding of SO_2 wall loss and the impact of RH (See *Supporting Information*), the SO_2 uptakes by the two types of aerosol particles under various conditions are compared. Fig. 3a summarizes the SO_2 decays during the NaCl and Chaka salts experiments under light and dark conditions at 4% RH, and the decay at 4% RH without particles is included as a reference. Compared to the reference (exp.6), all cases involving salt and SO_2 injections (exp.2-5) exhibit faster rates of SO_2 decay, showing additional uptake of SO_2 on salt particles. Since the RH is consistent across all cases, the difference in decay rates is solely attributed to the SO_2 uptake ability of the injected aerosol particles. Notably, except for the reference experiment, *i.e.*, without aerosol, the slowest decay rate is observed for the NaCl aerosol (red line), suggesting that the NaCl particles take up least SO_2. On the other hand, the Chaka salt, due to its complex composition (Liu et al., 2021), demonstrates a higher SO_2 uptake, as depicted by the blue solid and dashed curves, which correspond to two repeated experiments showing good reproducibility. The excess SO_2 uptake by natural salt particles, compared to NaCl, has been reported previously (Hoppel et al., 2001). The increased SO_2 absorption can be ascribed to several of the characteristics of the Chaka salt, including its enhanced chemical reactivity, greater surface area and porosity, and increased hygroscopicity. The light condition also influences the SO_2 uptake. As indicated by the green curve, when the light is on, the rate of SO_2 decay increases, suggesting that the SO_2 uptake by Chaka particles is enhanced under the light condition. Moreover, the enhanced SO_2 uptake is confirmed by the SEM-EDX results (Fig. 3b). This figure reveals that samples #2 to #4 exhibit comparably higher normalized sulfur concentrations under various conditions (SO_2 with 20% RH and light on/off, and SO_2 with 80% RH and light off) than sample #1, which was not exposed to SO_2. Notably, sample #5 displays an increased normalized sulfur concentration in conditions of 80% RH with light on. This suggests a notable enhancement in SO_2 uptake in conditions of high RH and light, as SO_2 is more effectively converted to sulfate in an aqueous environment when exposed to light.

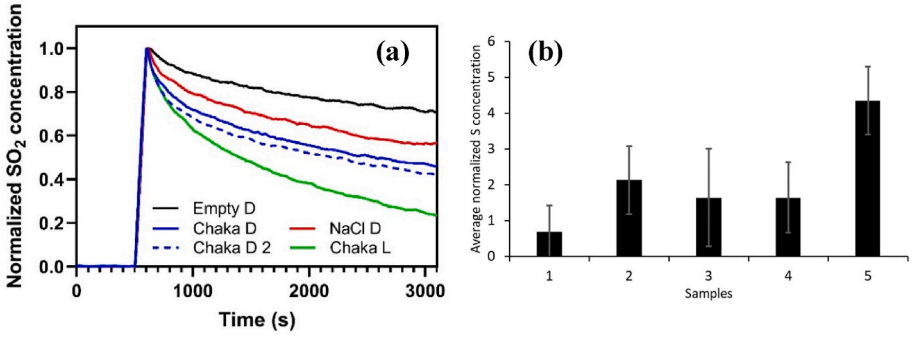

Fig. 3. (a) SO_2 decay in exp.2-6. The RH was 4% for all cases. D stands for dark condition, and L represents light condition. (b) Average normalized S concentration of five cases, based on SEM-EDX analysis. The samples are Chaka salts, and the conditions for each case are as follows. 1: 2% RH, no SO_2, light off. 2: 20% RH, 100 ppb SO_2, light off. 3: 80% RH, 100 ppb SO_2, light off. 4: 20% RH, 100 ppb SO_2, light on. 5: 80% RH, 100 ppb SO_2, light on.

3.2. Mass growth

The high hygroscopicity of salt particles is a significant characteristic that renders them active and influential in the climate system. In the CESAM experiments, the water uptake by salt particles was assessed by measuring mass concentrations, as shown in Fig. 4. The mass concentrations increase when the RH surpasses the deliquescence RH (DRH), *i.e.*, the threshold for solid salt particles transforming to droplets by absorbing water vapor. Pure NaCl is known to have a DRH of 75 % (Tang and Munkelwitz, 1993; Wise et al., 2007), as evidenced by the observation that the mass concentration only increases when the RH exceeds this value (Fig. 4a). On the other hand, Chaka salt, being a mixture, exhibits a lower DRH (Liu et al., 2021). The results presented in Fig. 5b demonstrate that the mass concentration already increases at an RH of 20% due to water uptake, and further increases as the RH continues to rise.

The presence of SO_2 has an impact on the hygroscopicity of salt particles. Fig. 4c illustrates that after exposure to SO_2, the Chaka particles experience a greater growth in mass concentration, which is also shown in Fig. 4e. Notably, the Chaka particles exhibit SO_2 uptake even at an RH of 4% (Fig. 3), indicating that the enhanced hygroscopicity arises from the surface modification by SO_2. Interestingly, when the light is on,

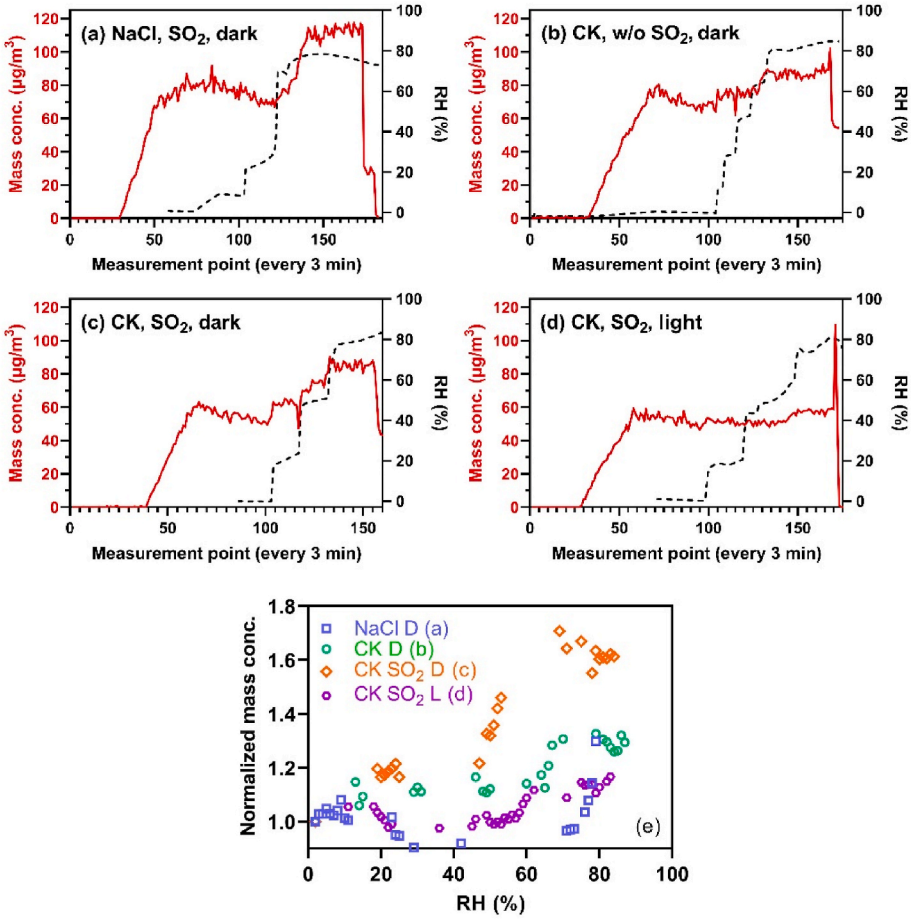

Fig. 4. (a–d) Mass concentration as a function of RH. (e) Relative mass growth as a function of RH, where the values are normalized to the first point, respectively. The letter D stands for dark condition and the letter L stands for light condition. Temporary dips in mass concentration are observed when RH increases, likely resulting from disturbances caused by water injection.

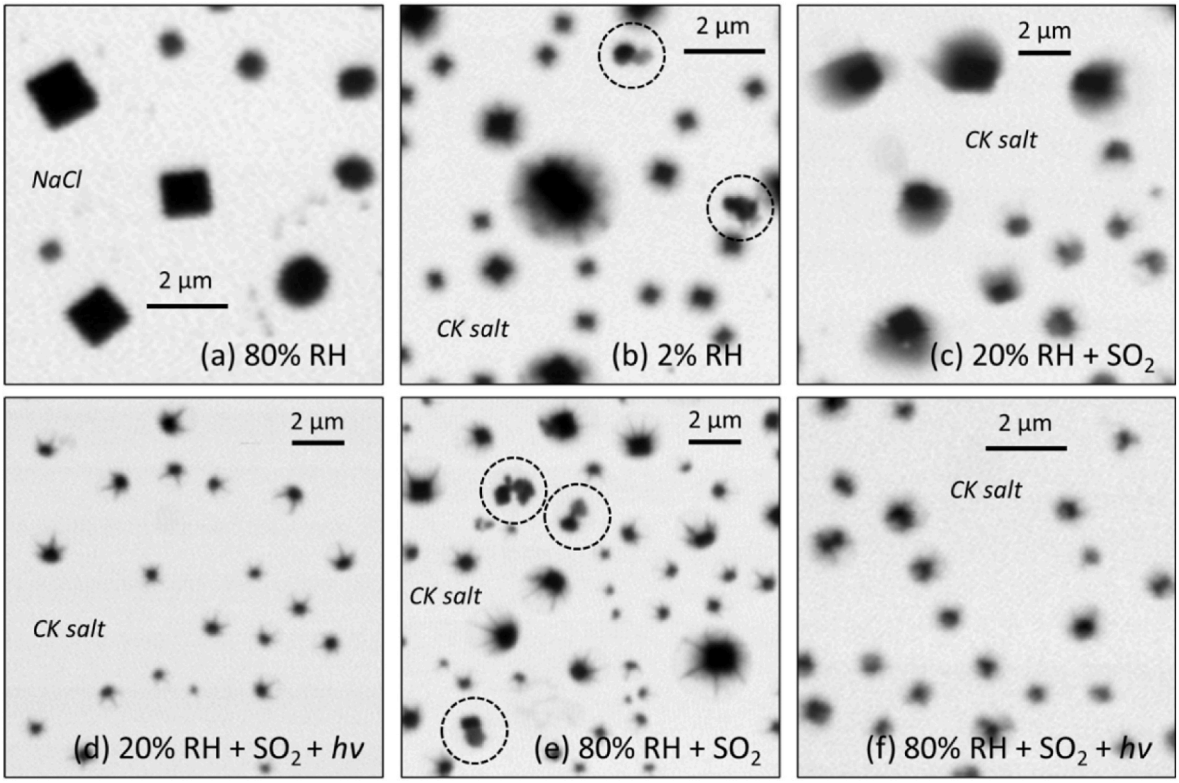

Fig. 5. Morphology of (a) NaCl particles and (b–f) CK salt particles, measured by STXM. The RH at the sampling moment is marked, and the presence of SO_2 and light is indicated. The photon energy is 300 eV for all cases.

the observed growth in mass concentration is significantly suppressed, as depicted in Fig. 5d and e. This is somehow surprising since the uptake of SO_2 is enhanced in the presence of light (Fig. 3). The suppressed mass growth indicates that formed species have a lower hygroscopicity. A slight increase is observed when the RH reaches 60%, but the observed mass growth is relatively modest. Regarding the enhanced SO_2 uptake and the available counterions, Na_2SO_4 is the most likely candidate compound that was formed. This hypothesis is also supported by the fact that Na_2SO_4 has a DRH higher than the maximum RH used in the experiments (Feng et al., 2014; Peng et al., 2022). Additionally, the introduction of sulfate ions leads to competition with chloride ions, resulting in the release of chlorine into the gas phase, likely as hydrochloric acid (HCl). A recent study showed that the surface of NaCl can be rapidly transformed to Na_2SO_4 upon SO_2 exposure, and the presence of light can accelerate this process (Kong et al., 2023). This matches the observation as NaCl is a major component in the Chaka salt mixture. In addition, similar phenomenon was observed on nitrate particles, where SO_2 reduced the hygroscopicity of $Ca(NO_3)_2$ particles due to formation of insoluble $CaSO_3$ or slightly soluble $CaSO_4$ (Yang et al., 2023).

3.3. Morphology and mixing state

3.3.1. Morphology

To understand how the Chaka salt differs from pure NaCl salt, and the effects of SO_2, RH and light condition, the morphology and mixing states of salt particles were examined by STXM. Fig. 5 shows the snapshots of the particles taken at a photon energy of 300 eV. A distinct difference is observed between the cubic-shaped NaCl crystals (Fig. 5a) and the Chaka salt particles (Fig. 5b), as the Chaka particles display a distinct structure consisting of cubic cores surrounded by coated materials (also see Fig. S3). The cubic core is most likely NaCl, agreeing with the fact that the Na^+ and Cl^- are saturated and the NaCl tends to precipitate out first from the Chaka brine, as indicated by calculations using the E-AIM model (Liu et al., 2021). Among the Chaka salt particles, several particles (circled) show different configurations, which appear to have cleaner boundaries without coatings. These particles have distinct chemical composition and will be discussed later.

The particles shown in Fig. 5c and d were collected at 20% RH, under light and dark conditions, respectively. An evident difference is that the particles collected under dark conditions (Fig. 5c) exhibit a cloud-like structure with thickness gradients, while the particles collected under light conditions (Fig. 5d) display distinct spike formations. This discrepancy may be attributed to the different physical properties of the particles when they were sampled. In Fig. 5c, the particles appear partially deliquesced, forming a slush-like mixture characterized by high viscosity. Consequently, when these particles effloresce on the TEM grid, the dissolved materials remain in position due to their low mobility. In contrast, the spikes observed in Fig. 5d are formed by fully deliquesced droplets with lower viscosity and higher mobility. When these droplets effloresce, the salt materials efficiently move and concentrate within the spike regions. Thus, the morphological disparity observed under light conditions suggest an enhanced hygroscopicity of Chaka salts, indicating more complete deliquescence. It should be noted that these particles were suspended in the chamber in the respective conditions for a significant period prior to sampling, allowing their physicochemical properties to reach equilibrium. Thus, the observed discrepancies are not a result of kinetic constraints leading to incomplete deliquescence but are indicative of the inherent hygroscopic properties of the particles. Fig. 6 provides an SEM image of the particles collected under the same conditions as Fig. 5d, clearly illustrating the presence of spikes as well as a ring structure, which represents the original size of the droplets upon collection.

However, the full deliquescence is in contrast with the total mass growth as depicted in Fig. 4, wherein the presence of light leads to a suppression of overall hygroscopicity. This phenomenon can potentially be attributed to the distinct chemical compositions and hygroscopic properties of Chaka particles based on their respective sizes. Comparing the particles in Fig. 5c and d, the particles in Fig. 5c are larger in size

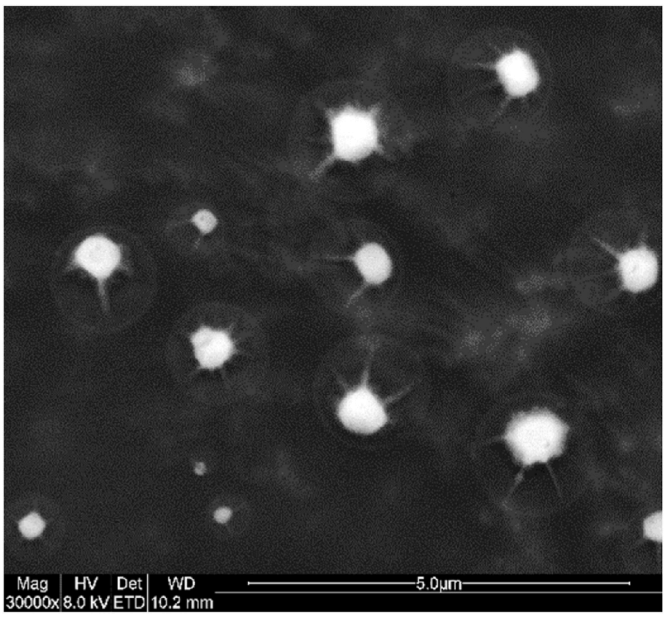

Fig. 6. SEM images of Chaka particles, sampled at 20% RH, after 100 ppb SO_2 exposure and light was on.

compared to those in Fig. 5d. As the mass concentration is more strongly influenced by larger particles rather than smaller particles, the diminished overall hygroscopicity could be attributed to the decreased hygroscopic behavior of the larger particles. While the smaller particles exhibit efficient water uptake, their impact on the overall mass concentrations is not significant. Nevertheless, these particles can substantially absorb water at RH at or lower than 20%. Given the ions present, it is plausible that these particles are primarily or partially composed of $MgCl_2$, as $MgCl_2$ particles are reported to exhibit DRH at ~16% (Gupta et al., 2015).

In Fig. 5e and f, the particles were collected at 80% RH, under dark and light conditions, respectively. Under dark conditions (Fig. 5e), the particles exhibit spike features, indicating full deliquescence of the salt particles. Some particles (circled) exhibit different shapes, which do not appear to be fully deliquesced. These particles may be Na_2SO_4 crystals, which will be explained in the following part. In Fig. 5f, despite of slight focus misalignment, all the particles in vision appear to be deliquesced, but the spikes are not as prominent as those observed under dark conditions.

3.3.2. *Mixing state*

With the power of chemical sensitivity, the mixing state of particles is also resolved by STXM. Fig. 7 showcases an example where Chaka particles were scanned using two photon energies: 525 eV (pre-edge of oxygen) and 537 eV (sulfate edge). At the pre-edge energy (Fig. 8a), oxygen-containing species are not activated, so the image reflects the overall X-ray adsorption by all elements present, with intensity scaled by the thickness of particles. In the image, most particles appear square-shaped, resembling the shape of NaCl crystals. Fig. 7b, corresponding to the sulfate edge at 537 eV, highlights the presence of sulfate. The sulfate edge exhibits a significant contrast compared to the pre-edge, and Fig. 7c presents a difference map between Fig. 8a and b, clearly showing that the sulfate presents as coatings surrounding NaCl crystals. The sulfate coatings are also confirmed by SEM-EDX measurements (Fig. S8), which shows that the sulfur content is higher on the edges compared to the center of particles.

Fig. 7c-f shows the differential maps for four conditions: (c) 2% RH, (d) 20% RH + 100 ppb SO_2, (e) 20% RH + 100 ppb SO_2 + light, and (d) 80% RH + 100 ppb SO_2. The pre-edge, sulfate-edge, and post-edge (measured at 550 eV) images can be found in Figs. S4-S7 in *Supporting Information*. As discussed already, at 20% RH with the presence of SO_2 but no light, the particles exhibit an ambiguous separation between the

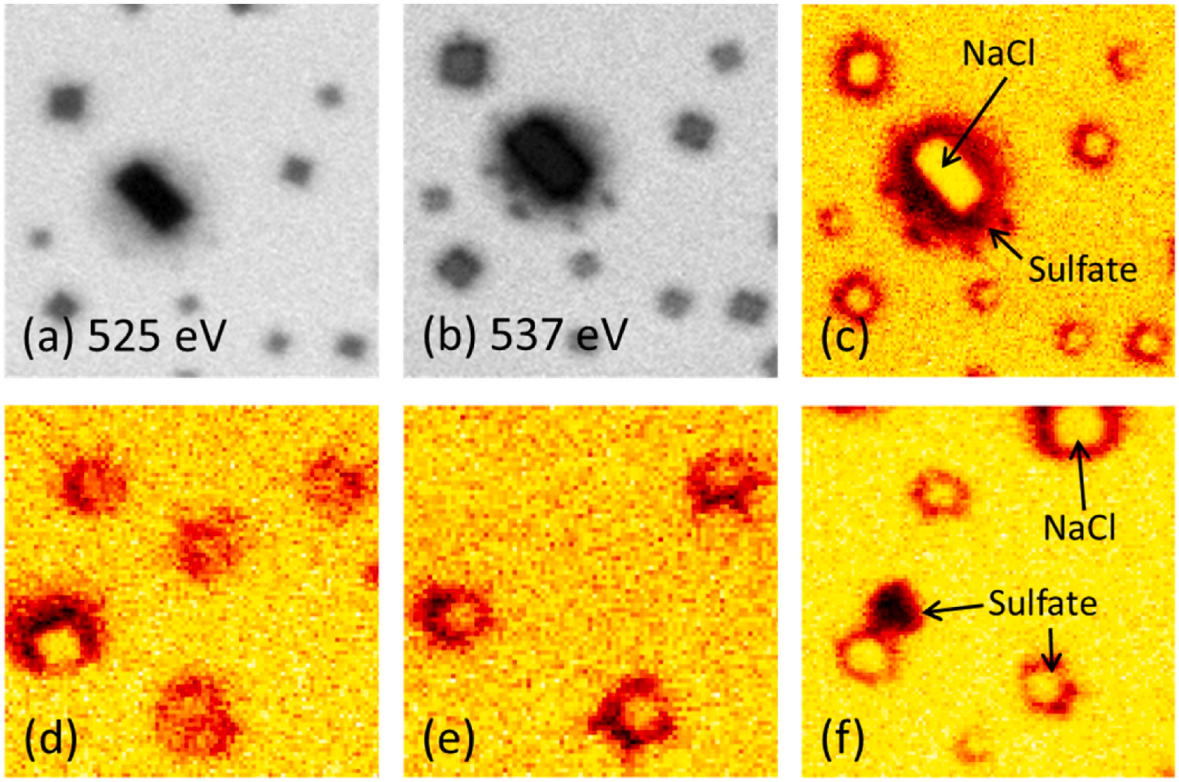

Fig. 7. STXM chemical mapping on oxygen K-edge: (a) pre-edge at 525 eV, (b) absorption of sulfate at 537 eV. (c–f) Difference maps between pre-edge and sulfate edge, where the distribution of sulfate is highlighted. (c) 2% RH, (d) 20% RH + SO_2, (e) 20% RH + SO_2 + light, (f) 80% RH + SO_2.

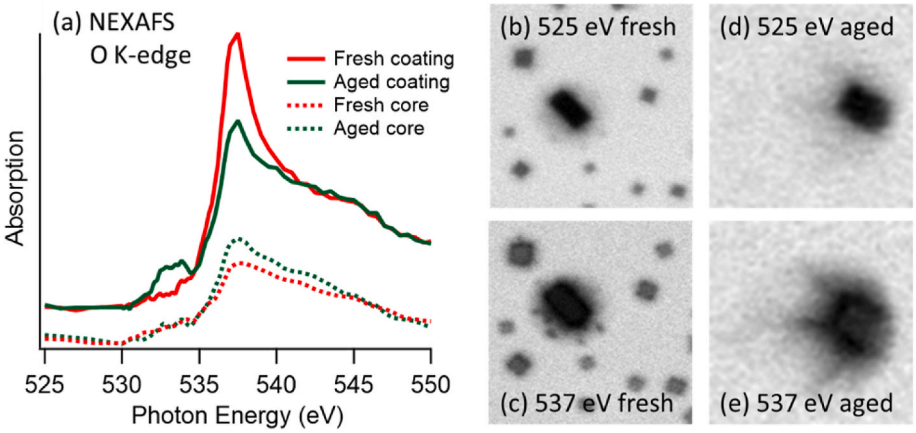

Fig. 8. (a) Oxygen K-edge NEXAFS spectra of fresh (red) and SO_2-aged (green) Chaka salt particles. The fresh particle was sampled at 4% RH, without SO_2 nor light exposures. The aged particles were collected at 80% RH, 100 ppb SO_2 injection, and the light was on. The spectra for the core and coating are shown in solid and dotted lines, respectively. The spectra are normalized to their pre-edge and post-edge. (b) and (c) show the pre-edge and sulfate-edge maps for the fresh particles, and (d) and (e) show the pre-edge and sulfate-edge maps for the aged particles. The core regions are defined as the center parts visible on the pre-edge (b and d), while the coating regions are defined as the new regions in the sulfate-edge map compared to the corresponding pre-edge maps.

core and coating materials. When exposed to light, the particles display spike-shaped coatings, and the coating-core separation becomes more apparent in Fig. 7e. In Fig. 7f, apart from well-separated sulfate-rich coatings, a standalone sulfate particle is observed, lacking a NaCl core but consisting entirely of sulfate throughout the particle. This sulfate particle could be Na_2SO_4, as this compound has a DRH higher than the RH during sampling, thereby showing no evidence of efflorescence on the TEM grid.

In addition to the differential mapping, full stack NEXAFS spectra were acquired at the oxygen K-edge for two cases: fresh Chaka particles sampled at 4% RH and aged (by both SO_2 and light) Chaka particles sampled at 80% RH, as shown in Fig. 8. The coating materials of fresh Chaka particles exhibit a distinct peak around 537 eV, corresponding to the presence of oxygen atoms in sulfate (Fauré et al., 2023; Kong et al., 2023; Priestley et al., 2023). In contrast, the core spectrum shows a less pronounced sulfate peak, supporting the conclusion that sulfate primarily exists as a coating surrounding the core, *i.e.*, NaCl, which does not contribute significantly to the oxygen spectrum. The formation of a NaCl core in particles originates from the Chaka brine being a solution saturated with NaCl. As a result, the first crystals to emerge from this brine are NaCl, as indicated in Liu et al. (2021). This leads to a nucleation process where NaCl crystals are commonly found at the center of mixed particles, with subsequent salts crystallizing around these cores, forming a coating. When Chaka particles are exposed to SO_2, light, and high RH (80%), the coating spectrum exhibits variations, where the sulfate peak at 537 eV decreases and an additional component emerges around 532–534 eV. This component may be associated with organics that exist in this particular particle, as the carbon K-edge NEXAFS spectra show that the aged particles (Fig. S10c) contain higher carboxylic components than the fresh particle (Fig. S9e). In addition, Figs. S9 and S10 show the NEXAFS spectra of other elements, including sulfur, chlorine, nitrogen, potassium and calcium. The sulfur, chlorine and potassium do not show significant differences between the fresh and aged particles, and intensities of nitrogen and calcium are very low.

This study provides pivotal insights into the mechanisms of SO_2 uptake and its subsequent conversion to sulfate on salt aerosol particles. The distinct uptake behaviors observed between the NaCl particles and the more complex Chaka salt particles highlight the pivotal role of specific ionic compositions, particularly in Chaka salt particles, in modulating SO_2 absorption. The Chaka salt particles, characterized by their multifaceted ionic compositions and pronounced hygroscopic attributes, notably exhibit enhanced SO_2 and water vapor uptake, it suggests that the surface environment, including ionic and water compositions, play a crucial role in enhancing the efficiency of SO_2 to sulfate transformation. Moreover, the observed alterations in mass growth in response to varying light conditions allude to that at the potential formation of species with specific ionic strengths, such as Na_2SO_4, which have implications for the overall SO_2-sulfate conversion rates in varying atmospheric conditions. The rounded shape and the unique structure of the Chaka salt particles, comprising cubic NaCl cores surrounded by sulfate coatings, further emphasize the interplay between ionic composition and the subsequent atmospheric reactions. This intricate relationship between particle morphology, ionic strength, and SO_2 uptake provides valuable insights into the broader dynamics of sulfate formation in the atmosphere, emphasizing the need to consider the ionic composition of aerosols when modeling and predicting atmospheric sulfate concentrations.

4. Conclusions

This study investigated the SO_2 uptake, hygroscopicity, morphology and mixing states of natural salt particles that are atomized from the brine sampled from Chaka salt lake. A comparison with atomized pure NaCl particles is included as reference. The results from this study show that NaCl is not a suitable proxy for such natural salt particles, neither in hygroscopic property, SO_2 absorption capacity, nor chemical morphological characteristics. The uptake of SO_2 by different salt particles under various conditions was examined, and the results show that the NaCl particles take up the lowest amount of SO_2, while the Chaka salt particles demonstrate higher uptake, due to their complex composition. The hygroscopicity of salt particles was affected by the chemical complexity, SO_2 exposure and light conditions. The Chaka salt shows higher hygroscopicity than pure NaCl, and the presence of SO_2 enhances the mass growth response of Chaka salt particles. However, mass growth is suppressed when light is on, suggesting the formation of species with lower hygroscopicity, such as Na_2SO_4. Even though the SO_2 uptake does not contribute to the mass directly, but the resulting surface transformation under light conditions can significantly change the hygroscopic property of the particles. This alteration can substantially impact the roles that these particles play in the atmosphere. The morphology and mixing states of the particles are analyzed, revealing distinct differences between NaCl crystals and Chaka salt particles. The Chaka salt particles exhibited a more rounded shape and a structure consisting of cubic NaCl cores surrounded by coated sulfate materials. Individual sulfate particles are also observed to externally mixed with internally mixed salt particles. The particles collected under different conditions

showed variations in deliquescence and efflorescence behavior, indicating the different status when the particles were sampled. The NEXAFS spectra show the different chemical fingerprints of fresh and aged particles, with the resolution of both core and coating regions.

CRediT authorship contribution statement

Xiangrui Kong: Writing – review & editing, Writing – original draft, Visualization, Validation, Supervision, Project administration, Methodology, Investigation, Funding acquisition, Formal analysis, Data curation, Conceptualization. **Cheng Wu:** Supervision, Investigation, Data curation. **Harsh Raj Mishra:** Data curation. **Yuxin Hao:** Data curation. **Mathieu Cazaunau:** Resources, Methodology, Investigation, Data curation, Conceptualization. **Antonin Bergé:** Investigation, Data curation. **Edouard Pangui:** Data curation. **Robin Faust:** Methodology, Investigation, Formal analysis, Data curation. **Wanyu Liu:** Methodology. **Jun Li:** Methodology. **Sen Wang:** Supervision, Resources, Project administration, Methodology. **Bénédicte Picquet-Varrault:** Writing – review & editing, Validation, Supervision, Resources, Project administration, Methodology, Investigation, Conceptualization. **Mattias Hallquist:** Writing – review & editing, Supervision, Resources, Project administration, Funding acquisition, Conceptualization.

Declaration of competing interest

The authors declare that they have no known competing financial interests or personal relationships that could have appeared to influence the work reported in this paper.

Data availability

The data is avaiable for download with a link.

Acknowledgements

This work is supported by the Swedish Research Council VR under contract 202104042. This work was also supported by the National Natural Science Foundation of China (41975160). X.K. acknowledges the support from the Swedish Foundation for International Cooperation in Research and Higher Education (CH2019-8361). This study is part of a Transnational access project that is supported by the European Commission under the Horizon 2020 – Research and Innovation Framework Programme, H2020-INFRAIA-2020-1, ATMO-ACCESS Grant Agreement number: 101008004. The ACTRIS-ASC DC unit is maintained by the French national center for Atmospheric data and services AERIS. A part of this work was performed at the BL4U of UVSOR Synchrotron Facility, Institute for Molecular Science (IMS program 22IMS6834).

Appendix A. Supplementary data

Supplementary data to this article can be found online at https://doi.org/10.1016/j.atmosenv.2024.120373.

References

Alcolombri, U., Ben-Dor, S., Feldmesser, E., Levin, Y., Tawfik, D.S., Vardi, A., 2015. MARINE SULFUR CYCLE. Identification of the algal dimethyl sulfide-releasing enzyme: a missing link in the marine sulfur cycle. Science 348, 1466–1469.
Alexander, B., Park, R.J., Jacob, D.J., Li, Q.B., Yantosca, R.M., Savarino, J., et al., 2005. Sulfate formation in sea-salt aerosols: constraints from oxygen isotopes. J. Geophys. Res. Atmos. 110.
Chen, Z., Liu, P., Wang, W., Cao, X., Liu, Y.X., Zhang, Y.H., et al., 2022. Rapid sulfate formation via uncatalyzed autoxidation of sulfur dioxide in aerosol microdroplets. Environ. Sci. Technol. 56, 7637–7646.
Cheng, Y., Zheng, G., Wei, C., Mu, Q., Zheng, B., Wang, Z., et al., 2016. Reactive nitrogen chemistry in aerosol water as a source of sulfate during haze events in China. Sci. Adv. 2, e1601530.
Dommer, A.C., Wauer, N.A., Angle, K.J., Davasam, A., Rubio, P., Luo, M., et al., 2023. Revealing the impacts of chemical complexity on submicrometer sea spray aerosol morphology. ACS Cent. Sci. 9, 1088–1103.
Elser, M., Huang, R.-J., Wolf, R., Slowik, J.G., Wang, Q., Canonaco, F., et al., 2016. New insights into $PM_{2.5}$ chemical composition and sources in two major cities in China during extreme haze events using aerosol mass spectrometry. Atmos. Chem. Phys. 16, 3207–3225.
Fauré, N., Chen, J., Artiglia, L., Ammann, M., Bartels-Rausch, T., Li, J., et al., 2023. Unexpected behavior of chloride and sulfate ions upon surface solvation of martian salt analogue. ACS Earth Space Chem. 7, 350–359.
Feng, X.-N., Chen, H.-N., Luan, Y.-M., Tan, S.-H., Pang, S.-F., Zhang, Y.-H., 2014. In-situ FTIR-ATR spectroscopic observation on the dynamic efflorescence/deliquescence processes of Na2SO4 and mixed Na2SO4/glycerol droplets. Chem. Phys. 430, 78–83.
Gaston, C.J., Pratt, K.A., Suski, K.J., May, N.W., Gill, T.E., Prather, K.A., 2017. Laboratory studies of the cloud droplet activation properties and corresponding chemistry of saline playa dust. Environ. Sci. Technol. 51, 1348–1356.
Ge, W., Liu, J., Xiang, S., Zhou, Y., Zhou, J., Hu, X., et al., 2022. Improvement and uncertainties of global simulation of sulfate concentration and radiative forcing in CESM2. J. Geophys. Res. Atmos. 127, e2022JD037623.
Ghomashi, F., Khalesifard, H.R., 2020. Investigation and characterization of atmospheric aerosols over the Urmia Lake using the satellite data and synoptic recordings. Atmos. Pollut. Res. 11, 2076–2086.
Gondwe, M., Krol, M., Gieskes, W., Klaassen, W., de Baar, H., 2003. The contribution of ocean-leaving DMS to the global atmospheric burdens of DMS, MSA, SO2, and NSS SO4. Global Biogeochem. Cycles 17 n/a-n/a.
Gupta, D., Eom, H.J., Cho, H.R., Ro, C.U., 2015. Hygroscopic behavior of NaCl–$MgCl_2$ mixture particles as nascent sea-spray aerosol surrogates and observation of efflorescence during humidification. Atmos. Chem. Phys. 15, 11273–11290.
Harris, E., Sinha, B., Hoppe, P., Foley, S., Borrmann, S., 2012. Fractionation of sulfur isotopes during heterogeneous oxidation of SO_2 on sea salt aerosol: a new tool to investigate non-sea salt sulfate production in the marine boundary layer. Atmos. Chem. Phys. 12, 4619–4631.
Hoppel, W., Pasternack, L., Caffrey, P., Frick, G., Fitzgerald, J., Hegg, D., et al., 2001. Sulfur dioxide uptake and oxidation in sea-salt aerosol. J. Geophys. Res. Atmos. 106, 27575–27585.
Kampf, C.J., Waxman, E.M., Slowik, J.G., Dommen, J., Pfaffenberger, L., Praplan, A.P., et al., 2013. Effective Henry's law partitioning and the salting constant of glyoxal in aerosols containing sulfate. Environ. Sci. Technol. 47, 4236–4244.
Kelly, J.T., Chuang, C.C., Wexler, A.S., 2007. Influence of dust composition on cloud droplet formation. Atmos. Environ. 41, 2904–2916.
Kong, X., Gladich, I., Faure, N., Thomson, E.S., Chen, J., Artiglia, L., et al., 2023. Adsorbed water promotes chemically active environments on the surface of sodium chloride. J. Phys. Chem. Lett. 14, 6151–6156.
Krishnamohan, K.-P.S.-P., Bala, G., Cao, L., Duan, L., Caldeira, K., 2019. Climate system response to stratospheric sulfate aerosols: sensitivity to altitude of aerosol layer. Earth System Dynamics 10, 885–900.
Kulmala, M., Pirjola, L., Makela, J.M., 2000. Stable sulphate clusters as a source of new atmospheric particles. Nature 404, 66–69.
Lai, A.C.K., Nazaroff, W.W., 2000. Modeling indoor particle deposition from turbulent flow onto smooth surfaces. J. Aerosol Sci. 31, 463–476.
Laskina, O., Morris, H.S., Grandquist, J.R., Qin, Z., Stone, E.A., Tivanski, A.V., et al., 2015. Size matters in the water uptake and hygroscopic growth of atmospherically relevant multicomponent aerosol particles. J. Phys. Chem. A 119, 4489–4497.
Lee, H.D., Wigley, S., Lee, C., Or, V.W., Hasenecz, E.S., Stone, E.A., et al., 2020. Physicochemical mixing state of sea spray aerosols: morphologies exhibit size dependence. ACS Earth Space Chem. 4, 1604–1611.
Li, W., Shao, L., Zhang, D., Ro, C.-U., Hu, M., Bi, X., et al., 2016. A review of single aerosol particle studies in the atmosphere of East Asia: morphology, mixing state, source, and heterogeneous reactions. J. Clean. Prod. 112, 1330–1349.
Liu, W., Li, J., Gu, W., Santos, L.F.E.D., Boman, J., Zhang, X., et al., 2021. Chemical and hygroscopic characterization of surface salts in the Qaidam Basin: implications for climate impacts on planet earth and mars. ACS Earth Space Chem. 5, 651–662.
Ohigashi, T., Arai, H., Araki, T., Kondo, N., Shigemasa, E., Ito, A., et al., 2013. Construction of the scanning transmission X-ray microscope beamline at UVSOR. J. Phys. Conf. 463, 012006.
Olson, N.E., May, N.W., Kirpes, R.M., Watson, A.E., Hajny, K.D., Slade, J.H., et al., 2019. Lake spray aerosol incorporated into great Lakes clouds. ACS Earth Space Chem. 3, 2765–2774.
Osler, W., 2012. The science of librarianship. University of Wales at Aberystwyth, July 31, 1917. J. Med. Libr. Assoc. 100. A.
Peng, C., Chen, L., Tang, M., 2022. A database for deliquescence and efflorescence relative humidities of compounds with atmospheric relevance. Fundamental Research 2, 578–587.
Pratap, V., Carlton, A.G., Christiansen, A.E., Hennigan, C.J., 2021. Partitioning of ambient organic gases to inorganic salt solutions: influence of salt identity, ionic strength, and pH. Geophys. Res. Lett. 48.
Priestley, M., Pei, X., Ohigashi, T., Yuzawa, H., Pettersson, J.B.C., Pathak, R.K., et al., 2023. Transformation of morphological and chemical properties by coating materials on soot. AIP Conf. Proc. 2990.
Quan, J., Liu, Q., Li, X., Gao, Y., Jia, X., Sheng, J., et al., 2015. Effect of heterogeneous aqueous reactions on the secondary formation of inorganic aerosols during haze events. Atmos. Environ. 122, 306–312.
Randles, C.A., 2004. Hygroscopic and optical properties of organic sea salt aerosol and consequences for climate forcing. Geophys. Res. Lett. 31.
Seinfeld, J.H., Pandis, S.N., 2016. Atmospheric Chemistry and Physics: from Air Pollution to Climate Change. Wiley.

Sullivan, R.C., Moore, M.J.K., Petters, M.D., Kreidenweis, S.M., Roberts, G.C., Prather, K. A., 2009. Effect of chemical mixing state on the hygroscopicity and cloud nucleation properties of calcium mineral dust particles. Atmos. Chem. Phys. 9, 3303–3316.
Tang, I.N., Munkelwitz, H.R., 1993. Composition and temperature dependence of the deliquescence properties of hygroscopic aerosols. Atmospheric Environment. Part A. General Topics 27, 467–473.
Thornhill, G.D., Collins, W.J., Kramer, R.J., Olivié, D., Skeie, R.B., O'Connor, F.M., et al., 2021. Effective radiative forcing from emissions of reactive gases and aerosols – a multi-model comparison. Atmos. Chem. Phys. 21, 853–874.
Urupina, D., Gaudion, V., Romanias, M.N., Thevenet, F., 2022. Surface distribution of sulfites and sulfates on natural volcanic and desert dusts: impact of humidity and chemical composition. ACS Earth Space Chem. 6, 642–655.
Wang, J., Doussin, J.F., Perrier, S., Perraudin, E., Katrib, Y., Pangui, E., et al., 2011. Design of a new multi-phase experimental simulation chamber for atmospheric photosmog, aerosol and cloud chemistry research. Atmos. Meas. Tech. 4, 2465–2494.
Wang, W., Liu, M., Wang, T., Song, Y., Zhou, L., Cao, J., et al., 2021. Sulfate formation is dominated by manganese-catalyzed oxidation of SO(2) on aerosol surfaces during haze events. Nat. Commun. 12, 1993.
Wang, T., Liu, M., Liu, M., Song, Y., Xu, Z., Shang, F., et al., 2022a. Sulfate Formation apportionment during winter haze events in North China. Environ. Sci. Technol. 56, 7771–7778.
Wang, T., Liu, Y., Cheng, H., Wang, Z., Fu, H., Chen, J., et al., 2022b. Significant formation of sulfate aerosols contributed by the heterogeneous drivers of dust surface. Atmos. Chem. Phys. 22, 13467–13493.
Wise, M.E., Semeniuk, T.A., Bruintjes, R., Martin, S.T., Russell, L.M., Buseck, P.R., 2007. Hygroscopic behavior of NaCl-bearing natural aerosol particles using environmental transmission electron microscopy. J. Geophys. Res. Atmos. 112.
Xingqi, L., Dong, H., Rech, J.A., Matsumoto, R., Bo, Y., Yongbo, W., 2008. Evolution of Chaka salt lake in NW China in response to climatic change during the latest pleistocene–holocene. Quat. Sci. Rev. 27, 867–879.
Yang, B., Xie, Z., Liu, J., Gui, H., Zhang, J., Wei, X., et al., 2023. Investigating the hygroscopicities of calcium and magnesium salt particles aged with SO(2) using surface plasmon resonance microscopy. Sci. Total Environ. 867, 161588.
Yu, J., Guo, Q., Gong, Y., Ding, L., Wang, J., Yu, G., 2021. A review of the effects of alkali and alkaline earth metal species on biomass gasification. Fuel Process. Technol. 214, 106723.
Yu, C., Liu, T., Ge, D., Nie, W., Chi, X., Ding, A., 2023. Ionic strength enhances the multiphase oxidation rate of sulfur dioxide by ozone in aqueous aerosols: implications for sulfate production in the marine atmosphere. Environ. Sci. Technol. 57, 6609–6615.
Zieger, P., Väisänen, O., Corbin, J.C., Partridge, D.G., Bastelberger, S., Mousavi-Fard, M., et al., 2017. Revising the hygroscopicity of inorganic sea salt particles. Nat. Commun. 8, 15883.